Dependence of band gaps in *d*-electron perovskite oxides on magnetism

Julien Varignon,[1] Oleksandr I. Malyi,[2] and Alex Zunger[2]

[1]*Laboratoire CRISMAT, Normandie Université, ENSICAEN, UNICAEN, Centre National de la Recherche Scientifique, 14000 Caen, France*

[2]*Renewable and Sustainable Energy Institute, University of Colorado, Boulder, Colorado 80309, USA*

(Received 4 June 2021; revised 24 December 2021; accepted 3 January 2022; published 7 April 2022)

In addition to the well-known dependence of band gaps of compounds on crystal symmetry and the orbital character of the constituent atoms, *d*-electron perovskites manifest an additional dependence of gaps on the magnetic spin configuration, a dependence deciding both metal-insulator transitions and magnetic application. We find via electronic structure theory that the factors that *explicitly* connect gapping magnitudes to magnetism depend on the nature of the band edge orbital character (BEOC) and scale with the number of antiferromagnetic contacts z_i between neighboring transition metal ions. The dependence is weak when the BEOC is (*d,d**)-like ("Mott insulators"), whereas this dependence is rather strong in (*p,d**)-like BEOC ("charge-transfer" insulators). These rather unexpected rules are traced to the reduced magnitude of interorbital interactions as the number of antiferromagnetic contacts z_i increases. In addition to these direct connections between magnetism and gaps, magnetic order also feeds back indirectly into the gapping problem by controlling the propensity of the lattice to develop lattice distortion. Such electronic instabilities toward Jahn-Teller distortions or bond disproportionation feed back into trends in band gap magnitudes. These results highlight the importance of establishing the appropriate magnetic order in the electronic structure theory for reliable rendering of gap-related phenomena such as doping, transport, metal-insulator transitions, and conductive interfaces.

DOI: 10.1103/PhysRevB.105.165111

I. INTRODUCTION

Oxide perovskites ABO_3 have long attracted broad interest thanks to their diverse range of properties encompassing ferroelectricity, magnetism, and superconductivity [1]. The band gap of perovskites stands out as one of its key quantities used not only to gauge metal-insulator transitions [2] and the physics of correlations [3], but also as basic features for designing catalysts, doping, transparent conductors, conductive interfaces, and switching of ferroelectrics. Thus, the ability of electronic structure theories to correctly track the band gaps of such solids—whether metals or insulators—has been a cornerstone of transition metal (TM) oxides science.

Perhaps the effect that held the community in the most fascination in this regard has been the persistent existence of insulating band gaps both in many (i) magnetically and crystallographically long-range ordered (LRO) ABO_3 phases as well as in (ii) paramagnetic phases lacking spin LRO phases (but having crystallographic LRO phases). Yet, simplified band theoretic models have repeatedly predicted a (false) metallic state in (i) and (ii), in conflict with established experiment, when the number of electrons per primitive cell is odd [4–6]. The traditional textbook explanation attributed this disagreement with experiment to the neglect of strong correlation in the mean-field band theoretic models. This view motivated historically the strong correlation physics approaches, encoded, e.g., in the celebrated Mott-Hubbard model [7,8] as an essential gap-opening mechanism in the otherwise false metals predicted by mean-field theories.

In the intervening years, however, it was understood that gapping in magnetically long-range ordered phases [(i) above] is explainable by antiferromagnetic (AFM) long-range spin order [9]—a spin symmetry breaking describable by mean-field-like band theory in low-temperature ground state phases of both binary (NiO, MnO) and ternary cases $NaOsO_3$ [10,11]. This necessitates, however, using a larger unit cell than the minimal size normally assigned. Furthermore, mean-field-like models lacking strong correlation [including density functional theory (DFT)] explained gapping in type (i) systems by positional *symmetry breaking* such as octahedral rotations, and others illustrated in Fig. 1, even in the absence of spin order [12–16]. Regarding category (ii) systems, it was recently understood that such gapping in paramagnetic phases is describable by allowing short-range ordered local magnetic moments without invoking strong correlation [11,17–19].

The physical picture emerging is that the initial attribution of the failure of mean-field approaches to predict gapping in (i) and (ii) was related to the traditional use of minimal size unit cells where the imposed high symmetry did not enable either positional or spin symmetry breaking even if they were to lower the total energy. Yet, now allowing supercells with constrained macroscopic shape (say cubic at high T and orthorhombic at low T), but letting the atoms and spins inside the supercell adopt locally their energy lowering configuration and using such structures in band theory, invariably shows gapping via mean-field approaches for both (i) and (ii). With this modern understanding of gapping in *d*-electron oxides we embark in this paper on the investigation of the dependence of band gaps in systems of type (i) on the nature of the spin order.

Trends in band gaps among different compounds are often divided according to the nature of the band edge orbital character (BEOC), as noted in *d*-electron oxides by Zaanen, Sawatzky, and Allen (see [20,21]). These band gaps are traditionally organized into three groups depending on BEOC: (i)

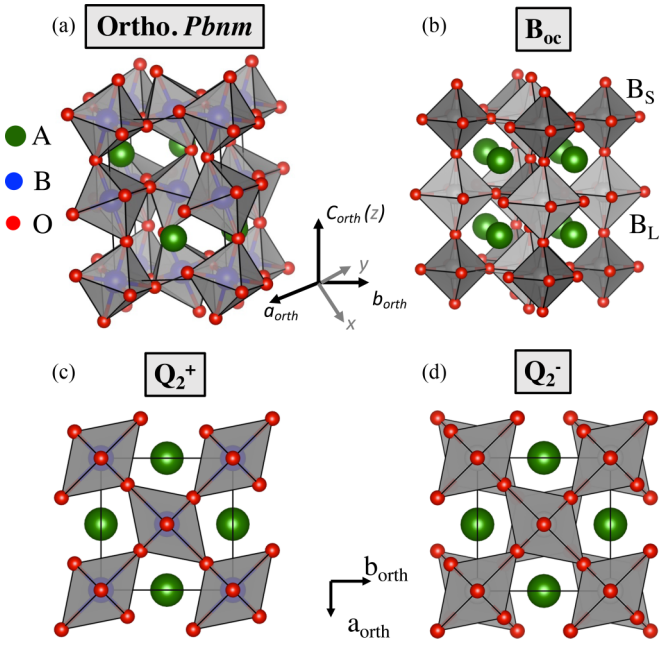

FIG. 1. Sketches of the perovskite structure and related structural distortions. (a) Orthorhombic *Pbnm* cell showing the usual $a^-a^-c^+$ octahedral rotations. (b) Bond disproportionation distortion B_{oc} splitting B sites into two groups, one sitting in compressed (Bi_S) octahedra and one sitting in extended octahedra (Bi_L). (c) Q_2^+ distortion with two B-O bond length contractions and extension in the (*ab*) plane with similar distortions between consecutive planes along the *c* axis. (d) Jahn-Teller Q_2^- distortions with B-O bond length contraction/extension alternating between all nearest-neighbor sites.

compounds where both the valence band maximum (VBM) and conduction band minimum (CBM) are predominantly made of the B atom *d* orbitals (d, d^*)—historically termed "Mott type compounds"; (ii) compounds where the VBM is made of anion *p* plus cation *d* orbitals and the CBM is made of majority cation *d* orbitals (p, d^*)—historically termed as "positive charge-transfer state"; and (iii) (p, p^*) compounds where the VBM and CBM are made of *p* orbitals—historically termed "negative charge-transfer" compounds. Classifications (i)–(iii) above complete the standard BEOC common in ordinary insulators of (iv) the VBM being anion *p* and the CBM being cation *s* denoted (p, s^*) band edges such as main group oxides and chalcogenides.

However, the aforementioned developments in understanding gapping mechanisms and type of *d*-electron ABO_3 perovskite oxides by symmetry breaking [12,17,18,22,23] face the unexplored role of magnetic interactions and various types of spin orders on the band gap amplitudes. Xiang *et al.* discussed that one-dimensional (1D), two-dimensional (2D), and three-dimensional (3D) AFM interactions in perfect 3D cubic lattices of spins could open and/or increase the band gap due to the increased compactness of bands with AFM interactions [24]. This type of transition from a metal to an insulator by going to an antiferromagnetic order is known as a Slater transition [9]. Also, trends in electronic properties of the particular series of lanthanides $LaBO_3$ (B = Sc to Cu) were discussed by He and Franchini [25]. However, the interplay between magnetic order vs positional symmetry breaking such as octahedral rotations, Jahn-Teller distortion, or bond disproportionation remains rather unexplored. Interestingly, we see, for instance, in Fig. 2 that the dependence of the DFT insulating gap on magnetic configurations is rather weak in Mott compounds, whereas this dependence is rather strong in charge-transfer insulators where the VBM is mostly formed by hybridized O-*p* and B-*d* states—and hence these are better labeled as compounds with (p-d,d^*) band edges.

We have investigated the impact of magnetism on the band gaps of *d*-electron perovskite oxides, finding unexpectedly that different band edge orbital character has different sensitivity to magnetism. The crucial correlative feature is the number of antiferromagnetic contacts between transition metal ions, and the causal mechanism establishing this correlation is explained. For instance, the dependence of the DFT insulating gap on magnetic configurations is rather weak in Mott (d,d^*) compounds, whereas this dependence is rather strong in charge-transfer (p,d^*) compounds. Uncovering this feature of gap vs magnetic configuration is important because it warns us of potential erroneous identification of rules or/and predictions of gapped or metallic materials using high throughput or machine learning techniques in which one may use an inappropriate magnetic order by convenience (smaller cell, higher symmetry, etc.). Here, we show that such trends in the magnitudes of insulating band gaps of ordered spin configurations scale with the number z_i of antiferromagnetic contacts between *i*th neighboring transition metal sites. This result is explained by the reduction in orbital interactions between neighboring TM sites through antiferromagnetic couplings. In some materials showing alternating occupied orbital patterns between nearest-neighbor sites forced by Jahn-Teller or bond disproportionation distortions, orbital interactions are already minimized, and only a specific magnetic order can maximize the band gap. The type of AFM interactions and band edges also controls the compacity of *d* states that in turn determines the ability of a material to show electronic instabilities toward a Jahn-Teller or disproportionation effect spontaneously. This realization clarifies how magnetism controls band gaps in perovskites having different band edge orbital characters. The importance of understanding such trends lies in the ability to control optical response, doping, catalysis, and band alignment at oxide interfaces by adjusting the band gap amplitude.

II. METHODS AND TECHNICAL DETAILS

A. The choice of the exchange-correlation functional

DFT calculations were performed with the Vienna Ab Initio Simulation Package (VASP) [26,27] with two functionals: (i) the generalized gradient approximation (GGA) PBEsol exchange-correlation functional [28] with an on-site U potential of 3 eV implement, acting on the 3*d* orbitals [29] in order to better cancel the spurious self-interaction errors inherent to approximate DFT [30], and (ii) the strongly constrained and appropriately normalized (SCAN, $U = 0$) [31] functional that does not involve any empirical parameter. No attempt is made here to optimize the constant U potential value for individual compounds as we are interested here in general metal vs insulator trends and overall scaling of insulating gaps

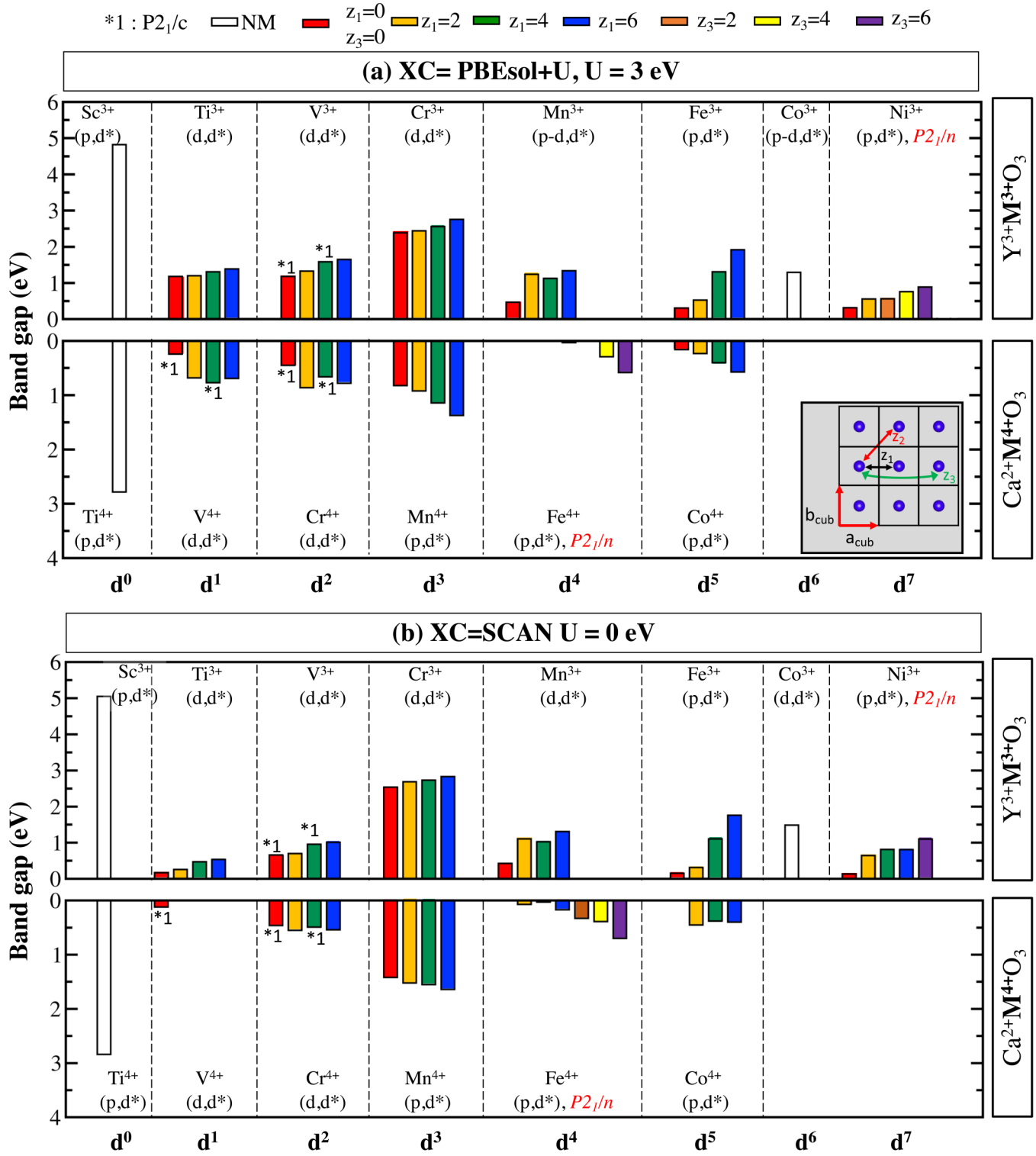

FIG. 2. Calculated DFT minimal energy single particle band gaps (in eV) displayed by ABO_3 perovskites as a function of the magnetic order described by the number z_i of AFM contacts for (a) PBEsol+U and (b) the SCAN functional. These include FM ($z_1 = 0$), AFMA ($z_1 = 2$), AFMC ($z_1 = 4$), AFMG ($z_1 = 6$), AFM2 ($z_3 = 2$), AFME ($z_3 = 4$), and AFMT ($z_3 = 6$) orders. NM stands for a non-spin-polarized calculation. The compounds shown have B atom electron count d^n, the average formal oxidation state being either in a 3+ (upper panel) or a 4+ (lower panel) crystal space group *Pbnm* except for $CaFeO_3$ and $YNiO_3$ that adopt the $P2_1/n$ symmetry and YVO_3, $CaCrO_3$, and $CaVO_3$ that adopt a $P2_1/c$ symmetry within specific magnetic orders. z_1, z_2, and z_3 are defined in the inset assuming a hypothetical high symmetry cubic cell for clarity. We use an on-site energy $U = 3$ eV for all cases for DFT+U calculations, avoiding fitting individual cases. This U value might be overestimated for $CaVO_3$ that we find insulating while it is a metal experimentally. A lower U value was previously fitted to 1.25 eV [17]. Band edges are determined using the band structures reported in Appendix.

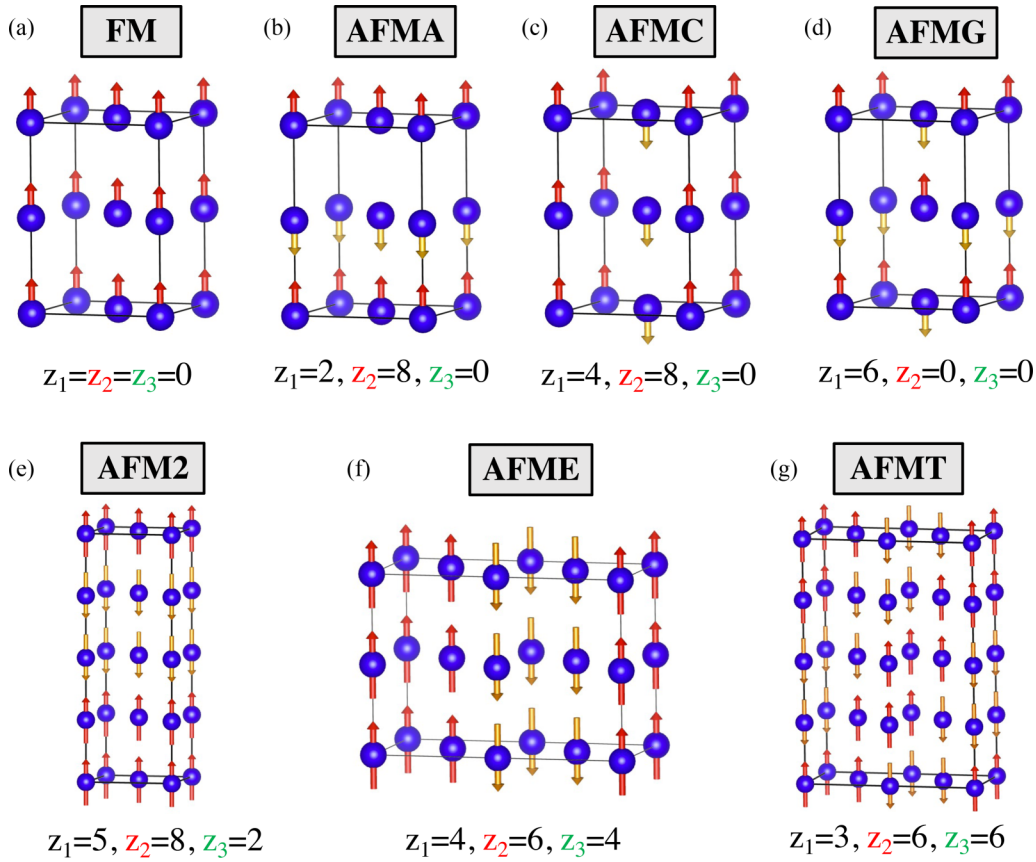

FIG. 3. Sketches of the different magnetic type of order used in the present calculations. Here, z_1, z_2, and z_3 are the number of AFM contacts between first-, second-, and third-nearest-neighbor transition metal sites.

with physical descriptors such as the number of AFM contacts rather than fitting experiment. We note in passing that, likely due to an inappropriately large U potential, $CaVO_3$ is found insulating, while it is a metal experimentally [32] (U was fitted to 1.25 eV in a previous study [17]). A similar explanation may stand for $CaCrO_3$, although it is not clear experimentally if it is a metal or an insulator [33,34].

B. Testing types of magnetic order

To define the different types of magnetic order used in the calculations we introduce the notion of a number of nearest neighbors (NNs) between spins located at the TM elements that are coupled antiferromagnetically, up to the third NN. Here, z_1 is the number of first-NN TM sites coupled antiferromagnetically. The maximum value of z_1 can be 6. In turn, z_2 is the number of second-NN AFM interactions, and its maximal value is 12. Finally, z_3 is the number of AFM contacts between third-NN TM elements. The maximal value of z_3 is 6. Based on z_1, z_2, and z_3, we can define several types of magnetic order. In most cases, magnetic interactions can be restricted to first NN, such as in ferromagnetic (FM) ($z_1 = 0$), A-type AFM (AFMA, $z_1 = 2$), C-type AFM (AFMC, $z_1 = 4$), and G-type AFM (AFMG, ($z_1 = 6$) [Figs. 3(a)–3(d)]. For materials showing disproportionation effects, magnetic interactions have to be considered up to second- and third-NN spins because of the existence of a rock salt pattern of different spin amplitudes [Fig. 1(b)]. These AFM interactions between second and third NN are considered within the AFM2 ($z_3 = 2$), AFME ($z_3 = 4$), and AFMT ($z_3 = 6$) ordering. Note that we label these three latest types of order in terms of z_3 instead of z_2 since third-NN interactions should be dominant: going through an intermediate site, AFM interaction for z_3 contact would be along a line (favoring AFM interactions) while AFM interactions for second-nearest neighbors would form a 90° configuration, rather weakening AFM interactions.

C. Structural relaxation

Crystallographic cells used in the calculations correspond to a few cases:

(i) Orthorhombic *Pbnm* symmetry (4 f.u./cell) allows the $a^-a^-c^+$ octahedral rotations in Glazer's notation [35], e.g., $YScO_3$, $YTiO_3$, $YCrO_3$, $YFeO_3$, $YCoO_3$, $CaTiO_3$, $CaMnO_3$, and $CaCoO_3$ [see Fig. 1(a) for the sketch of the distortion].

(ii) Lower symmetry $P2_1/c$ space groups are caused by the potential appearance of Jahn-Teller distortion Q_2^-, e.g., YVO_3, $CaVO_3$, and $CaCrO_3$ within given magnetic orders.

(iii) $P2_1/n$, e.g., $CaFeO_3$ and $YNiO_3$, symmetries allow a bond disproportionation B_{oc} distortion mode [see Figs. 1(d) and 1(b) for a sketch of distortions, respectively].

The input defining the orthorhombic cell corresponds to a $(\sqrt{2}a_{cub}, \sqrt{2}a_{cub}, 2a_{cub})$ supercell (4 f.u.) with respect to the primitive, undistorted, cubic cell having a a_{cub} lattice parameter [see Fig. 1(a)]. The 4 f.u. cell is compatible with the usual FM, AFMA, AFMC, and AFMG magnetic ordering

(i.e., $z_1 = 0$ to 6). Nevertheless, other magnetic ordering with $z_3 \neq 0$ such as AFMT requires a (2,1,2) orthorhombic supercell, i.e., 16 f.u. Full structural relaxation (lattice parameters and atomic positions) is performed until forces acting on each atom are lower than 1 meV/Å.

D. Probing electronic instabilities with the SCAN $U = 0$ exchange-correlation functional

In [11,17,22], potential electronic instabilities, either of the Jahn-Teller or a disproportionation type, were probed by computing total energies of cubic cells in two ways: (i) imposing equal occupation numbers in degenerate partners such as (1/2, 1/2) for a single electron for doubly degenerate e_g orbitals or (ii) using integer occupancy of a specific degenerate partner—such as (1,0) for e_g levels. The latter case can break the symmetry. If an electronic instability exists, then state (ii) should yield lower energy than state (i). Nevertheless, this is only feasible for DFT functionals able to differentiate between occupied and unoccupied states. DFT+U is able to probe electronic instabilities [11,17,22]. Meta-GGA functionals such as SCAN $U = 0$ cannot detect electronic instabilities in undistorted cells with degenerate partners. We have thus employed another strategy to seek for electronic instabilities. We plot potential energy surfaces as a function of structural distortions such as Jahn-Teller or bond disproportionation starting from the cubic cell in order to observe a shifted single well to nonzero amplitude, indicating the presence of an electronic instability lowering the total energy.

E. Other technical details

Other relevant computational DFT details are that the plane-wave basis cutoff energy is set to 500 eV and that $5 \times 5 \times 3$ *and* $3 \times 5 \times 2$ gamma centered k meshes are used for the 4- and 16-f.u. supercells, respectively. Projector augmented wave (PAW) [36] potentials are used for modeling core electrons, and we explicitly treat p and d electrons for all TM elements. Symmetry mode analysis for extracting amplitude of distortions was performed with the AMPLIMODES application of the Bilbao crystallographic server [37,38]. Potential energy surfaces have been computed starting from a (2,2,2) cubic supercell (8 f.u.) in which we freeze Q_2^+ and Q_2^- mode amplitudes with frozen lattice vectors. We kept the 16-f.u. supercell for the B_{oc} mode. In both 8 and 16 f.u. supercell cases, the k mesh has been increased to $5 \times 5 \times 5$ and $4 \times 6 \times 3$, respectively. Band unfolding is performed with the VASP Band Unfold code using the strategy presented in [39] and bands are projected on B-d and O-p states in order to determine band edges. Band structures are provided in the Appendix.

F. Wannier function analysis

Wannier functions (WFs) were built from DFT Bloch band structure both with PBEsol+U and SCAN-no-U functionals. Depending on the compounds we use the low-temperature orthorhombic $Pbnm$, $P2_1/c$, or $P2_1/n$ space group symmetries to build O-p and B-d atomiclike orbitals. Within an orthorhombic cell containing 4 f.u., for instance, we thus seek to build 4×5 d-like and 12×3 p-like WFs, i.e., a total of 56 WFs. To that end, we project the 56 Kohn-Sham states located around the Fermi level that always have dominant O p- and B d-like character on initial atomic orbitals of p and d characters centered on O and TM ions, respectively, to extract the initial gauge matrix for the localization procedure. WFs are then optimized through spread minimization as implemented in the WANNIER90 package [40–42]. Each atomiclike energy is then extracted from the on-site potential associated with each optimized WF.

III. RESULTS

A. Classification of oxide perovskites according to the orbital character of their band edges using Wannier energies

The classification of the type of band gaps traditionally proposed is based on semiempirical approaches (such as tight-binding models [20,21]), where the chemical trends are not always faithfully reproduced because of the need of using fixed rather than self-consistent parameters. To characterize the different band edge orbital types self-consistently from DFT, we computed the charge-transfer energy ΔE_{dp}, i.e., the energy difference between TM d states and anion O p states using Wannier functions built from our DFT Bloch band structure both with PBEsol+U and SCAN-no-U functionals. The *charge-transfer energy* ΔE_{dp} is then defined as the difference between the average diagonal matrix element of d-like WFs $\underline{E_d}$ and p-like WFs $\underline{E_p}$, i.e., $\Delta E_{dp} = \underline{E_d} - \underline{E_p}$.

Figure 4 depicts the calculated Wannier charge-transfer energy ΔE_{dp} as a function of the number of unpaired electrons on the transition metal d orbitals for both PBEsol+U and SCAN functionals. Both functionals provide similar trends for ΔE_{dp}. However, a global shift of about 1 eV to higher energies is observed for the SCAN functional for transition metal elements from Sc to Fe. As a result, $YMnO_3$ falls within the Mott insulator classification with the SCAN functional, while it is rather a charge-transfer insulator in PBEsol+U—we observe larger p-d hybridization at the VBM with the PBEsol+U functional than with the SCAN functional although band edges remain rather (d,d*) for both functionals. However, $|\Delta E_{dp}|$ is close to zero with both functionals and $YMnO_3$ is more likely located on the verge of the two regimes. Regarding global trends, we see that the sign change of ΔE_{dp} marking the transition from Mott-like to charge-transfer-like behavior is governed by the (i) addition of electrons on d orbitals at a fixed formal oxidation state (FOS) and (ii) the increase of the formal oxidation state of a fixed B cation that both produce a systematic shift of ΔE_{dp} to lower energies. Interestingly, a low or high spin state affects the type of band edge orbital type. We see that $YNiO_3$ with seven d electrons but with only one (expected) spin unpaired electron due to a low spin state is at the verge between charge-transfer and Mott insulator regimes with both PBEsol+U and SCAN but with a charge-transfer energy ΔE_{dp} that is nearly zero [also reflected by the observation of (p-d,p-d*)-like band edges in Fig. 2]. At the same time, $YFeO_3$, with a smaller number of d electrons but with a high spin state and five spin unpaired electrons, is a charge-transfer insulator with both functionals with a large, negative, ΔE_{dp}. Figure 4 thus defines a DFT predictor for classifying compounds into different BEOC

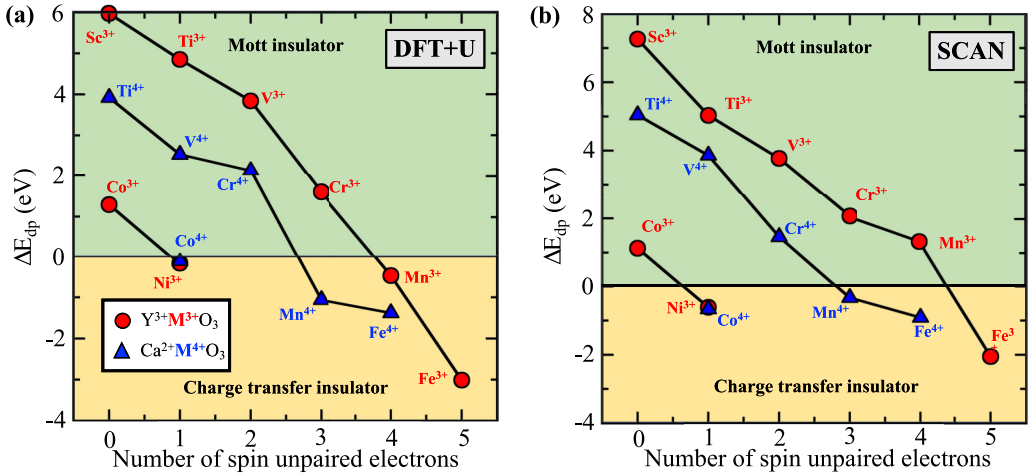

FIG. 4. Wannier charge-transfer energy ΔE_{dp} (in eV) (difference between metal d- and anion p-like Wannier function energies) as a function of the number of unpaired electrons on each B cation in either a 3+ (red filled squares) or a 4+ (blue filled triangles) formal oxidation state for (a) DFT+U and (b) SCAN simulations. The transition between the Mott insulator and charge-transfer insulators occurs when ΔE_{dp} changes the sign. We have used the AFMG magnetic order ($z_1 = 6$) for all compounds, except FM $YTiO_3$ ($z_1 = 0$), AFMT for $YNiO_3$ and $CaFeO_3$ ($z_3 = 6$), and nonmagnetic $CaTiO_3$, $YScO_3$, and $YCoO_3$. We note here that due to a d^0 electronic count, $CaTiO_3$ and $YScO_3$ are usual band insualtors with a gap formed between occupied O-p states and unoccupied d states.

categories without relying on semiempirical parametrization [20,21].

B. DFT predicted trends in band gap magnitudes for different band edges and magnetic configurations

For orthorhombic (*Pbnm*) and monoclinic ($P2_1/c$ or $P2_1/n$) structures, we report in Fig. 2 the band gap value as a function of the d electron count for different number z of AFM contacts between nearest-neighbor sites for both PBEsol+U and SCAN functionals. Both functionals provide similar trends; however, $CaVO_3$ is predicted metallic with most magnetic states except the FM case with the SCAN functional while DFT+U produces an insulating phase whatever the magnetic order is—likely coming from a too large U potential (see Sec. II).

Several trends, encodable in rules that are explained later in the paper, emerge:

(i) Compounds adopting an orthorhombic cell whatever the magnetic order (i.e., $YTiO_3$, $YCrO_3$, $YFeO_3$, $CaMnO_3$, $YCoO_3$, and $CaCoO_3$) have the largest gaps when all first-NN spins are antiferromagnetically coupled (i.e., $z_1 = 6$, being AFMG order).

(ii) The gap increases monotonically with increasing number z_1 of AFM contacts for compounds adopting a low-temperature *Pbnm* symmetry. This is independent of the BEOC.

(iii) Compounds with (d, d*) band edges (Mott insulators) such as 3+ FOS (i.e., $YTiO_3$, YVO_3, and $YCrO_3$) show a rather weak increase in gap with the number z_1 of AFM contacts between first-nearest-neighbor sites. The slope is large for (p-d, d*) charge-transfer compounds such as the late transition metal oxide perovskites $YFeO_3$ and for perovskites with a 4+ FOS (i.e., $CaMnO_3$ and $CaCoO_3$).

(iv) Compounds that can exhibit a lower symmetry (e.g., monoclinic structure either $P2_1/c$ or $P2_1/n$ rather than the orthorhombic *Pbnm* symmetry) have band gaps that are larger not for $z_1 = 6$ but for $z_3 = 6$ (i.e., $CaFeO_3$ and $YNiO_3$), $z_1 = 2$ (i.e., $CaCrO_3$), or $z_1 = 4$ (i.e., $CaVO_3$).

C. Understanding the origin of band gap increase with increasing number of AFM contacts in orthorhombic *Pbnm* structures

To understand how the band gap increases with the number z_1 of first-NN AFM contacts, we consider the projected density of states (PDOS) on B d and O p levels as a function of z_1 for our DFT+U method. Figure 5 shows this PDOS for $YFeO_3$. Considering a 3D network of ferromagnetically coupled Fe spins (FM states, $z_1 = 0$), the band gap E_g is small, but the bandwidth W associated with the t_{2g} states in the unoccupied manifold is rather large ($W = 1.8$ eV). Upon adding 1D, 2D and 3D AFM networks, one observes that E_g increases and at the same time W decreases. The largest DFT gap ($E_g = 1.92$ eV) and the smallest bandwidth ($W = 0.65$ eV) are reached for a purely 3D network of AFM interactions between nearest-neighbor sites (i.e., AFMG, $z_1 = 6$).

The scaling of gaps with the number of AFM contacts z_1 originates from d orbital interactions between nearest-neighbor transition metal sites that are related to the transfer integral t_{dd} following [24]. In the solid, the strength of the orbital interaction between two neighboring sites is directly given by t_{dd} for FM interactions, but it is related to ${t_{dd}}^2/U$ for an AFM interaction, where U is the energy cost of locating two electrons in the same orbital. In practice, t_{dd} is much larger than ${t_{dd}}^2/U$ and t_{dd} is related to the transfer integral t_{pd} between O p and TM d states through the relation $t_{dd} = \frac{t_{pd}^2}{\Delta E_{pd}}$ (i.e., superexchange mechanism [43]). We report in Figs. 6(a) and 6(b) the orbital interaction between two neighboring sites occupied by a single electron located in the same orbital $\emptyset_a$ for a FM and an AFM situation. Before interactions between

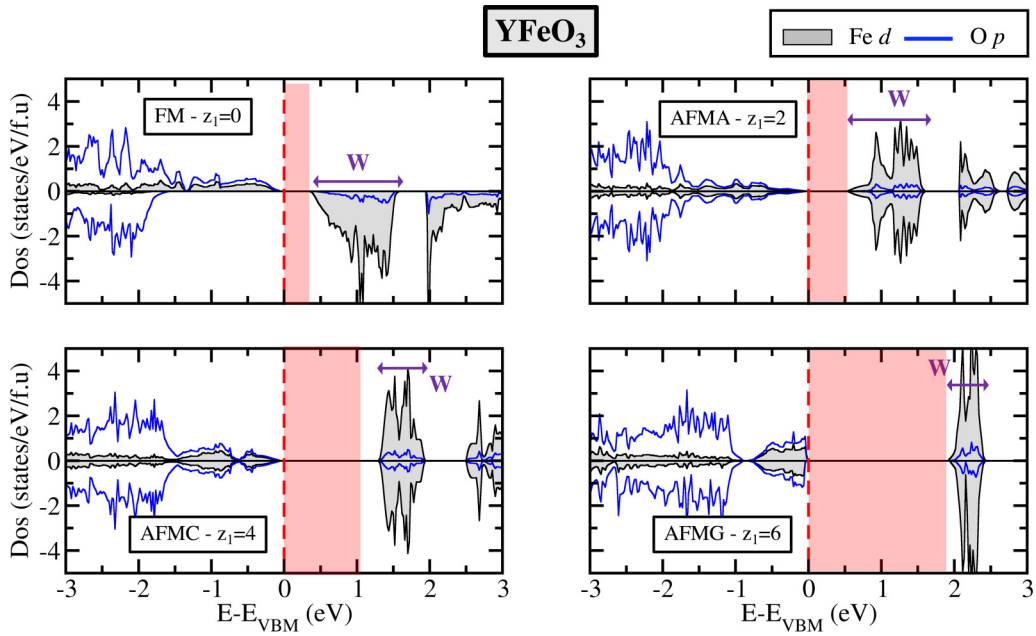

FIG. 5. Projected density of states on B d (filled gray) and O p (blue line) states in $YFeO_3$ for different magnetic orders. The DFT+U results are used here. The band gap is highlighted by the red area and the bandwidth W of unoccupied t_{2g} states is highlighted by arrows.

neighboring sites, the gap is initially given by the exchange splitting Δ_{ex} separating spin up and spin down orbitals locally on each TM. Recalling that only orbitals of similar spin can interact together, orbital interactions thus induce a broadening of the bands either diminishing the band gap by $2t_{dd}$ for a FM configuration or increasing the band gap by $2{t_{dd}}^2/U$ for an AFM interaction as sketched in Figs. 5(a) and 5(b). Thus, the gap for a given magnetic configuration with z_1 AFM contacts between first-nearest-neighbor sites can be written as

$$E_g(z_1) = \Delta_{ex} - 2(6 - z_1)t_{dd} + 2z_1\frac{t_{dd}^2}{U} \tag{1}$$

It follows from Eq. (1) that

$$E_g(0) = \Delta_{ex} - 12t_{dd} \tag{2}$$

for a FM solution (i.e., $z_1 = 0$) whereas

$$E_g(6) = \Delta_{ex} + 12{t_{dd}}^2/U \tag{3}$$

for an AFMG solution (i.e. $z_1 = 6$).

Figure 7(a) shows the gap variation ΔE_g as a function of the number z_1 of AFM interactions introduced in $YTiO_3$, $CaCoO_3$, $YCrO_3$, $CaMnO_3$, and $YFeO_3$ for the PBEsol+U

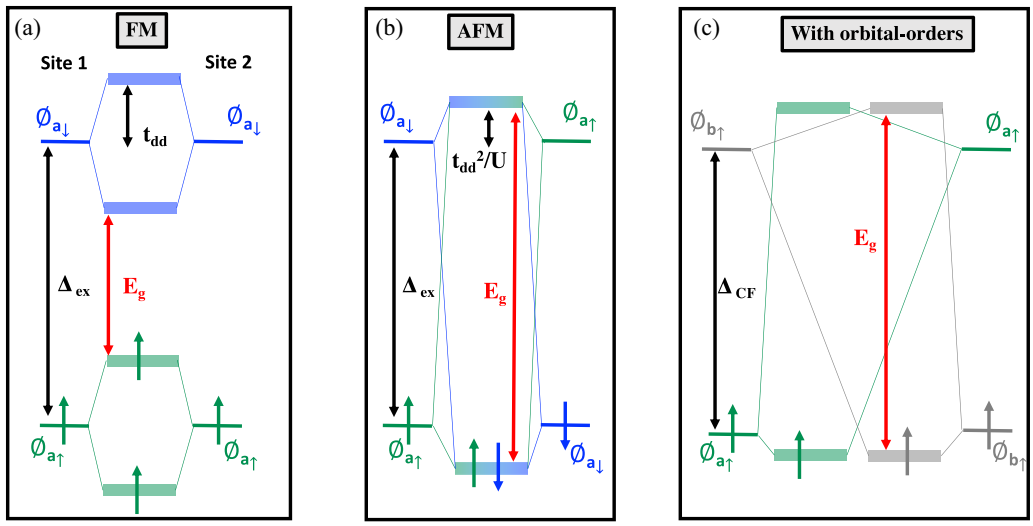

FIG. 6. (a, b) Sketches of interactions between similar orbitals $\emptyset_a$ for a (a) FM arrangement and (b) AFM arrangement on neighboring transition metal sites. Only one orbital is considered. Spin up and down channels are split by the exchange splitting Δ_{ex}. (c) Sketches of interactions between two different occupied orbitals $\emptyset_a$ and $\emptyset_b$ for a material showing an orbital arrangement on neighboring sites. The orbitals locally on each site are now split by the crystal field Δ_{CF}.

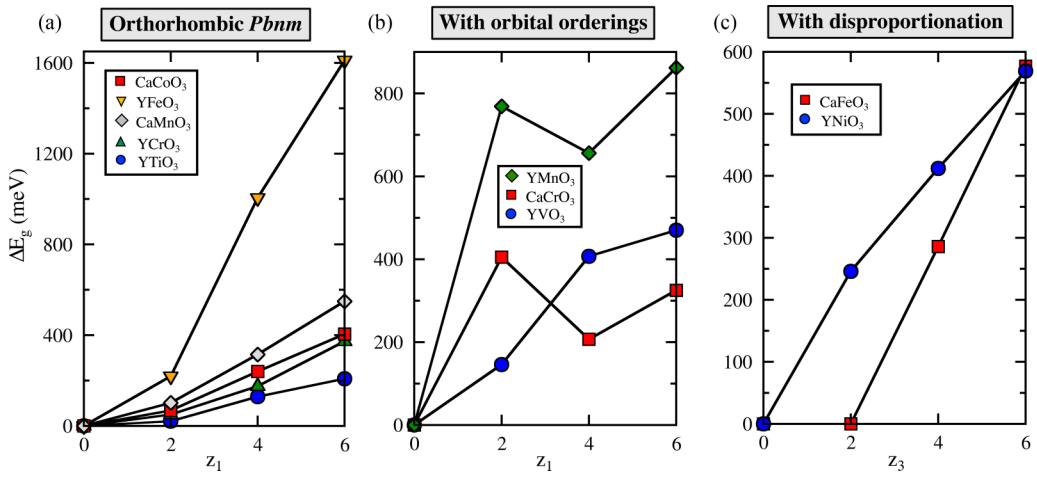

FIG. 7. Band gap variation as a function of the number of AFM contacts z_1 in compounds (a) adopting the *Pbnm* structure and (b) showing the additional Q_2 modes and (c) as a function of z_3 in materials showing disproportionation effects. The DFT+U results are used here.

results. As one can see, the band gap increases upon adding more AFM interactions, similar for all compounds, *modulo* an amplitude that becomes larger when going from Mott insulators to charge-transfer insulators ($YTiO_3$ vs $CaCoO_3$ or $YFeO_3$, $YCrO_3$ vs $CaMnO_3$). This is understandable for $YTiO_3$ ($YFeO_3$) in which the occupied t_{2g} (e_g) orbital has a small (large) overlap with O p states thereby producing a weak (large) t_{pd} and thus t_{dd}. At a fixed magnetic moment but at different FOS such as in $YCrO_3$ and $CaMnO_3$, the effective integral t_{dd} also depends on the relative TM d and O p energy positions ΔE_{dp} ($t_{dd} \propto \frac{1}{\Delta E_{dp}}$) [21]. Since Δ E_{dp} is slightly smaller for $CaMnO_3$ than for $YCrO_3$ (Fig. 2), t_{dd} is thereby slightly larger for $CaMnO_3$. Consequently, the positive contribution ${t_{dd}}^2/U$ to E_g is larger.

As inferred by Fig. 3, the trend is similar for the SCAN functional albeit (i) band gaps are smaller with respect to DFT+U, as notable in $YTiO_3$, or (ii) gap renormalization with magnetic order can be less pronounced as in $CaMnO_3$. The former discrepancy (i) comes from the tendency of SCAN to underestimate band gaps with respect to DFT+U or hybrid DFT while the latter discrepancy (ii) can possibly originate from the SCAN tendency to overestimate magnetism, magnetic energies, and magnetic moments as suggested in [18,44,45].

D. Lattice distortions lowering the orthorhombic *Pbnm* symmetry induce different orbital occupancies on nearest neighbors

As shown in Fig. 2, some compounds deviate from the trend of a monotonic gap evolution with the number of AFM contacts z_1 and with the largest value for $z_1 = 6$. This is the case for YVO_3, $CaCrO_3$, $YMnO_3$, $CaFeO_3$, and $YNiO_3$ that show additional and sizable deformation modes with respect to the conventional *Pbnm* symmetry (see Table I). These modes are (i) the bond disproportionation mode B_{oc} in $CaFeO_3$ and $YNiO_3$; (ii) the ${Q_2}^+$ octahedral deformation mode in YVO_3 (AFMA and AFMG orders, i.e, $z_1 = 2$ and 6, respectively), $CaCrO_3$ (AFMA and AFMG orders), and $YMno_3$ (all magnetic states); and (iii) the Jahn-Teller mode ${Q_2}^-$ mode for YVO_3 and $CaCrO_3$ (FM and AFMC with $z_1 = 0$ and 4, respectively). Whatever the origin of these modes, electronically induced or structurally triggered [17,22,23,46–49], different orbital occupancies between neighboring sites emerge, ultimately modifying magnetic interactions between TM elements (e.g., Goodenough-Kanamori rules [43,50]).

In disproportionating materials such as $YNiO_3$ and $CaFeO_3$, two different magnetic sublattices forming a rocksalt pattern are enabled by the bond disproportionation (breathing) mode B_{oc} [Fig. 1(b)]. In the low-temperature insulating phase, the rocksalt pattern imposes alternating ${e_g}^2/{e_g}^0$ occupancies between NN transition metal sites. In order to apply the mechanism discussed in orthorhombic *Pbnm* cells, orbital interactions between similarly occupied orbitals can only be accounted for for third-NN neighbors—second NNs form a 90 ° angle and are not considered dominant (see Sec. II). With an AFMG order, third-NN interactions are all ferromagnetic ($z_3 = 0$) and thus the order does not minimize orbital interactions between TM sites belonging to the same magnetic sublattice. Substantial minimization of band broadening is realized when TM ions of the same magnetic sublattice are AFM coupled ($z_3 = 6$) in a similar spirit of band broadening minimization when only first-NN interactions are important. This is verified with our calculations: $YNiO_3$ and $CaFeO_3$ indeed show the largest gap value for when the number z_3 of

TABLE I. Amplitude (in Å) of octahedral distortions extracted from a symmetry mode analysis with respect to the primitive high symmetry *Pm*-3 cubic cell. Results are presented for DFT+U results.

	${Q_2}^+$ (Å)			${Q_2}^-$ (Å)		B_{oc} (Å)	
	YVO_3	$CaCrO_3$	$YMnO_3$	YVO_3	$CaCrO_3$	$YNiO_3$	$CaFeO_3$
$z_1 = 0$	0.028	0.001	0.142	0.051	0.041	0.082	0.043
$z_1 = 2$	0.079	0.047	0.142				
$z_1 = 4$	0.030	0.002	0.158	0.051	0.045		
$z_1 = 6$	0.078	0.056	0.160				
$z_3 = 2$						0.089	0.046
$z_3 = 4$						0.095	0.061
$z_3 = 6$						0.094	0.068

AFM contacts between third NNs reaches its maximal value of 6 as shown by Fig. 7(c).

Some other materials such as YVO_3, $YMnO_3$, and $CaCrO_3$ prefer to show alternating orbital occupancies between some nearest-neighbor transition metal sites such as alternating ${d_x}^2/{d_y}^2$ occupied orbitals in the (ab) plane in $YMnO_3$. In this case, we have to consider interactions between two different $\emptyset_a$ and $\emptyset_b$ orbitals between NN sites. The situation for a single electron per site is sketched in Fig. 6(c), with a gap now initially given by the crystal field splitting Δ_{CF} separating the two orbitals $\emptyset_a$ and $\emptyset_b$ locally on each site. Due to the different occupied orbitals $\emptyset_a$ and $\emptyset_b$ between neighboring sites, orbital interactions produce a diagram similar to the AFM case with identical occupied orbitals [Fig. 6(b)] but irrespective of the presence of an AFM order. In fact, the number of neighboring sites with orthogonal orbital occupancy is here the primary key factor for maximizing the band gap. One can even notice that, unlike the situation presented for orthorhombic materials without "orbital orderings," a FM interaction would even maximize the band gap with respect to an AFM coupling since orbital interactions are greater for FM than for AFM (i.e., t_{dd} is greater than ${t_{dd}}^2/U$).

The number of orthogonal orbital occupancies between neighboring sites is given by the type of Q_2 mode: for ${Q_2}^+$, only NN (ab)-plane TM sites show alternating orbital occupancies while the ${Q_2}^-$ mode forces alternating occupancies in all three directions. Thus, the former distortion minimizes orbital interactions for only four of six nearest-neighbor sites while the latter minimizes orbital interactions for all six NNs. It follows that adding an AFM coupling along the c axis for compounds showing the ${Q_2}^+$ such as $YMnO_3$ or $CaCrO_3$ should supply the remaining gap maximization/bandwidth minimization. This is verified in our simulations for $YMnO_3$ and $CaCrO_3$ [Figs. 2 and 7(b)] in which the largest gap values are reached for the AFMA and AFMG magnetic orders showing an AFM coupling along the c axis. Materials exhibiting the ${Q_2}^-$ mode should, in principle, exhibit a gap independent of magnetic orders. However, due to strongly coupled structural-spin-orbital orders, the ${Q_2}^+$ mode is favored by octahedral rotation and is connected to AFMA and AFMG orders in YVO_3 (see [22] for a complete, detailed demonstration). This material, therefore, exhibits an AFMG order in the low-temperature phase experimentally [51,52] for which the band gap is maximized—the (ab)-plane AFM contacts come from the fact that the d_{xy} orbital is occupied on all V sites and hence provides a gap increase.

IV. DISCUSSION

A. The gap is necessarily smaller in charge-transfer insulators than in Mott insulators

In the description of band gaps with a number of AFM contacts, we have neglected the role of the charge-transfer energy on the amplitude. Starting from a Mott insulator with a large, positive, charge-transfer energy ΔE_{dp}, d states are above the O p states. Thus, one expects that the initial gap before the interaction is linked to the exchange splitting Δ_{ex} or crystal field splitting Δ_{CF} locally on each site (i.e., when $\Delta E_{dp} > \Delta_{ex}/2$ or $\Delta E_{dp} > \Delta_{CF}/2$). Upon decreasing ΔE_{dp}, O p states can be located between occupied and unoccupied d orbitals, or even above both orbitals for large, negative ΔE_{dp} (i.e., when $\Delta E_{dp} < \Delta_{ex}/2$ or $\Delta E_{dp} < \Delta_{CF}/2$). Thus, the initial gap has to be given by Δ_{ex} or Δ_{CF} minus a contribution from ΔE_{dp}. We indeed systematically observe a global shift of the band gap amplitude to lower values upon decreasing the charge-transfer energy at fixed d-electron count such as in $YScO_3$ vs $CaTiO_3$ or $YCrO_3$ vs $CaMnO_3$.

B. Magnetic effects on the additional structural distortion amplitudes

For any of the materials, we do not observe a noticeable variation of the octahedral rotation mode or antipolar motions of A site cations with the number of AFM contacts. Nevertheless, octahedral deformation modes such as ${Q_2}^+$, Jahn-Teller ${Q_2}^-$, or bond disproportionation B_{oc} possess an amplitude that strongly varies with the number of AFM contacts z_1 or z_3 (see Table I). We indeed observe that (i) the ${Q_2}^-$ mode is only enabled with FM ($z_1 = 0$) and AFMC ($z_1 = 4$) orders for YVO_3 and $CaCrO_3$ for instance, i.e., magnetic orders with a FM coupling between TM ions along one crystallographic direction, with a constant amplitude of 0.051 Å for YVO_3 and a slightly varying amplitude of 0.041 Å (FM, $z_1 = 0$) and 0.045 Å (AFMC, $z_1 = 4$) for $CaCrO_3$; (ii) the ${Q_2}^+$ mode is sizable and large only with AFMA and AFMG orders (i.e., $z_1 = 2$ and 6, respectively) for YVO_3 and $CaCrO_3$, albeit the ${Q_2}^+$ amplitude increases with the number of AFM contacts in the latter compound, and large and rather constant as a function of z_1 for $YMnO_3$; and (iii) the bond disproportionation amplitude varies with the number of third-NN AFM contacts in $YNiO_3$ ($CaFeO_3$), being 0.082 (0.043) Å, 0.089 (0.046) Å, 0.095 (0.061) Å, and 0.094 (0.068) Å for z_1 and $z_3 = 0$, $z_3 = 2$, $z_3 = 4$, and $z_3 = 6$, respectively.

While the connection between magnetic orders and the ${Q_2}^+$ or the Jahn-Teller ${Q_2}^-$ mode was explained by Kugel and Khomskii [53,54], we clearly observe that, once induced, the amplitude of these distortions is rather independent of the AFM or FM nature of couplings between TM elements for compounds showing *(d,d*)* BEOCs. In compounds showing *(p-d,d*)* BEOCs such as $CaFeO_3$, $CaCrO_3$, or $YMnO_3$, the dependence of the additional octahedral deformations becomes strongly connected to the number of relevant AFM contacts. Thus, magnetic effects are not restricted to the gap amplitude but are also directly related to the distortion amplitude associated with the gap opening process in perovskite oxides [12,17,18,22].

C. Magnetic effects on electronic instabilities and consequences on Jahn-Teller and disproportionation effects

It was previously established that Jahn-Teller ${Q_2}^-$ and bond disproportionation B_{oc} distortion originate from an electronic instability while ${Q_2}^+$—appearing in the rare-earth manganites or titanates—is just consequential of octahedral rotations [17,22]. The absence of electronic instabilities in rare-earth titanates and manganites is ascribed to insufficiently localized d states, i.e., states with a large bandwidth, thereby screening any potential electronic instability [22]. We have checked the presence of potential electronic instabilities in our

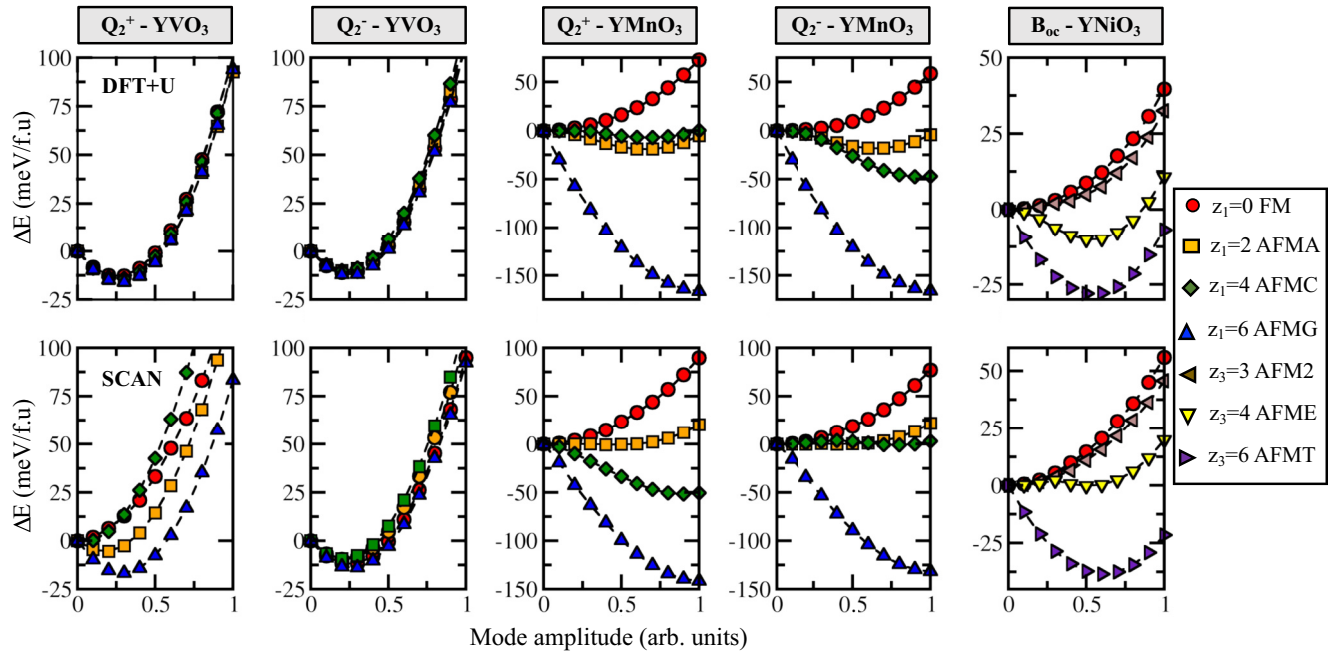

FIG. 8. Magnetic dependent potential energy surfaces associated with the Q_2^+, Q_2^-, and B_{oc} modes in YVO_3, $YMnO_3$, and $YNiO_3$ starting from a perfectly cubic cell. Results are reported for DFT+U (upper panels) and SCAN-no-U (lower panels) functionals. The reference energy is set at zero amplitude of the distortion.

simulations by plotting potential energy surfaces as a function of Q_2^+, Q_2^-, and B_{oc} modes for each relevant magnetic state starting from a cubic cell for YVO_3, $YMnO_3$ (both Q_2^+ and Q_2^- modes), and $YNiO_3$ (B_{oc} mode), both with PBEsol+U and SCAN functionals. Figure 8 depicts the potential energy surfaces associated with the distortions as a function of the number of AFM contacts z_1 and z_3.

For the Q_2^+ and Q_2^- modes in YVO_3, we observe a single-well potential whose minimum is located at nonzero amplitude of the modes whatever the magnetic order for DFT+U, thus signaling an electronic instability toward a Jahn-Teller effect. With the SCAN functional, the Q_2^- mode is always associated with a shifted single-well potential whatever z_1 while for the Q_2^+ mode only AFMA ($z_1 = 2$) and AFMG ($z_1 = 6$) can detect the shifted single-well potential. These observations confirm that (i) the Q_2^- mode minimizes orbital interactions whatever the magnetic order and produces already compact states and thus electronic instabilities are directly observed while (ii) the AFM coupling between similarly occupied orbitals along one direction for the Q_2^+ mode produces more compact states than with FM and AFMC orders, thus allowing the electronic instability—this is particularly true with the SCAN functional that produces less compact states than DFT+U.

Results are different in $YMnO_3$ for both DFT+U and SCAN functionals and both Q_2^+ and Q_2^- modes: (i) a FM ($z_1 = 0$) order yields a single-well potential whose energy minimum is located at zero amplitude of the modes, (ii) AFMA and AFMC ($z_1 = 2$ and 4) lead to a double-well potential with a minimum located at nonzero amplitude of the modes, and (iii) a shifted single-well potential to finite amplitudes of Q_2^+/Q_2^- modes is observed with the AFMG order. Thus, $YMnO_3$ and related manganites such as $LaMnO_3$ would exhibit an electronic instability yielding a Jahn-Teller effect only if spin interactions are all AFM between NN sites ($z_1 = 6$), i.e., the state with the most compact d states as shown in Fig. 5. This is in good agreement with the conclusions expressed in [22] and with the calculations of the electronic instabilities in the PM cell of [17], where it was found that states are insufficiently localized in rare-earth manganites to sustain a Jahn-Teller distortion. Instead, the stabilization of Q_2^+ is assisted by spin interactions as shown by the double-well potentials for AFMA and AFMC orders plus a coupling with the $a^-a^-c^+$ octahedral rotation pattern [22,47].

Regarding the disproportionation effect in $YNiO_3$, different results are observed depending on the magnetic order: (i) a single-well potential centered at zero is obtained for FM ($z_1 = 0$, $z_3 = 0$) or AFM2 states ($z_3 = 2$), (ii) a double-well potential is observed for the AFME ($z_3 = 4$) order, and (iii) a shifted single-well potential is observed once sufficient AFM interactions are considered ($z_3 = 6$, i.e., AFMT). Again, once d states become more compact and localized, an electronic instability yielding disproportionation effects appears. This is consistent with calculations using AFMT and PM cells from [17,23].

D. Implications of the dependence of electronic instabilities with magnetism on the origin of the metal-insulator transition of $RNiO_3$ compounds

Mercy *et al.* proposed that the metal-insulator transition in $RNiO_3$ materials is structurally triggered by the octahedral rotations [23]: based on potential energy surface plots

of the B_{oc} mode at fixed rotation amplitude using a simple FM simulation, they observed that increasing the octahedral rotation amplitude softens the B_{oc} mode and hence it can be stabilized for sufficiently large rotations irrespective of the presence of PM or AFM orders. The scenario is convenient as it explains why compounds with large rotation such as $YNiO_3$ can transform from a paramagnetic metal to a paramagnetic insulator as the temperature goes down, and that this is impossible for $NdNiO_3$ and $PrNiO_3$ that both show smaller O_6 rotations. Ultimately, these two compounds become insulating at the AFM transition as it is observed experimentally [55,56]. Yet, an electronic instability toward disproportionation of the unstable 3+ formal oxidation state of Ni cations is identified based on DFT calculations and dynamical mean-field calculations in the PM cell of nickelates [17,57,58].

Our observation of a bandwidth dependent electronic instability—through the number of relevant AFM contacts—yielding a disproportionation effect in $YNiO_3$ reconciles the two physical observations and explains the phase diagram of rare-earth nickelates: (i) large O_6 rotations produce compact d states in early nickelate members and thus disproportionation effects can appear irrespective of the magnetic order such as in the PM cell for $RNiO_3$ with R = Y, Lu-Sm but (ii) in materials lacking large rotations such as $NdNiO_3$ and $PrNiO_3$ AFM interactions improve the compacity of Ni d states and hence the electronic instability toward disproportionation is restored at the AFM transition.

In conclusion, the metal-insulator transition in rare-earth nickelates is related to an electronic instability whose strength is connected to d-level bandwidth. The latter is directly related to octahedral rotation amplitude (a structural factor) and the type of relevant magnetic interactions.

V. CONCLUSIONS

We have shown that magnetism through making states more compact upon increasing the number of AFM contacts acts on band gap amplitudes and intrinsic electronic instabilities. Compounds showing orbital orderings already minimize some orbital interactions and thus only AFM couplings between nearest sites showing the same orbital occupancies are required to maximize the band gap. It follows that potential consequences of magnetism on band gaps and perovskite properties are as follows.

(i) Electronic instabilities opening band gaps could be missed or identified if an irrelevant magnetic order is used in the simulation.

(ii) Intermediate states in the gap or polaron formation upon doping a perovskite could be missed if a FM state is used due to a strong gap underestimation as well as over delocalized electronic structures.

(iii) Band alignments at oxide interfaces and associated charge transfer could be incorrectly simulated by restricting DFT simulations with a FM order, notably at the oxide interface between (d,d*) and (p-d,d*) BEOCs compounds where the band gap and related lattice distortions may be dramatically underestimated in the charge-transfer insulator.

(iv) False gap closure under epitaxial strain or pressure effects could be observed if the incorrect magnetic order is used, notably with a FM order in which the starting gap and related lattice distortions are already way too underestimated in the bulk phase.

(v) This thus warns against using the data available in open-access materials databases (e.g., Materials Project [59], OQMD [60,61], and AFLOW [62]), which all in most cases are limited to ferromagnetic calculations.

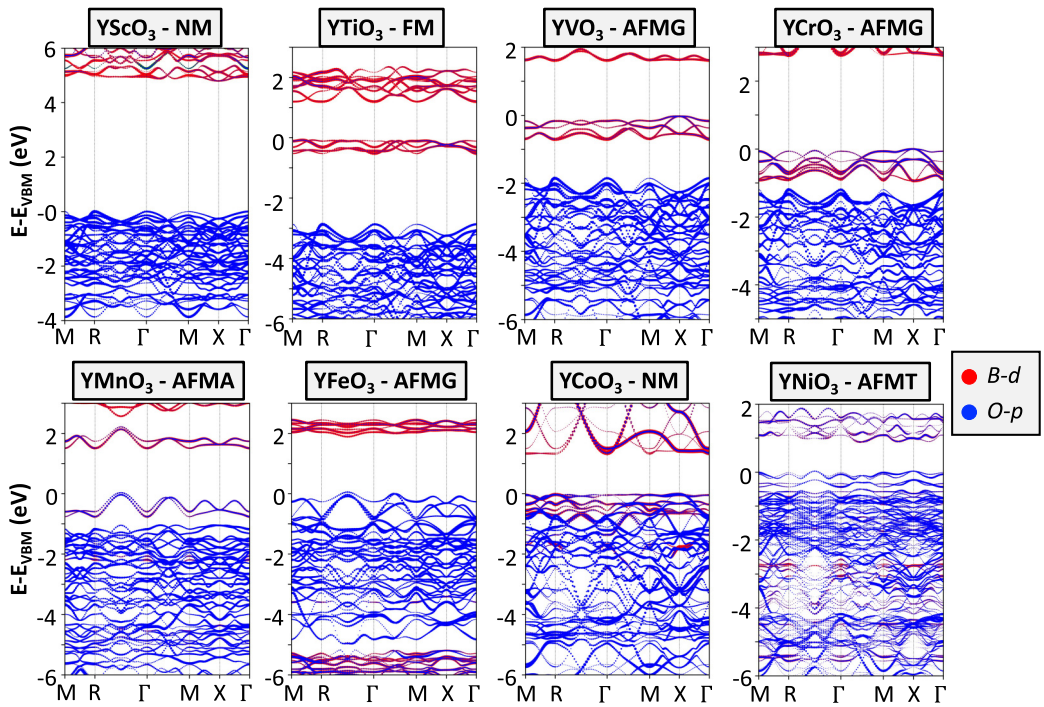

FIG. 9. Unfolded band structures of YBO_3 compounds projected on the transition metal B d states (in red) and O p states (in blue). DFT+U results are used here. Only the majority spin channel is reported.

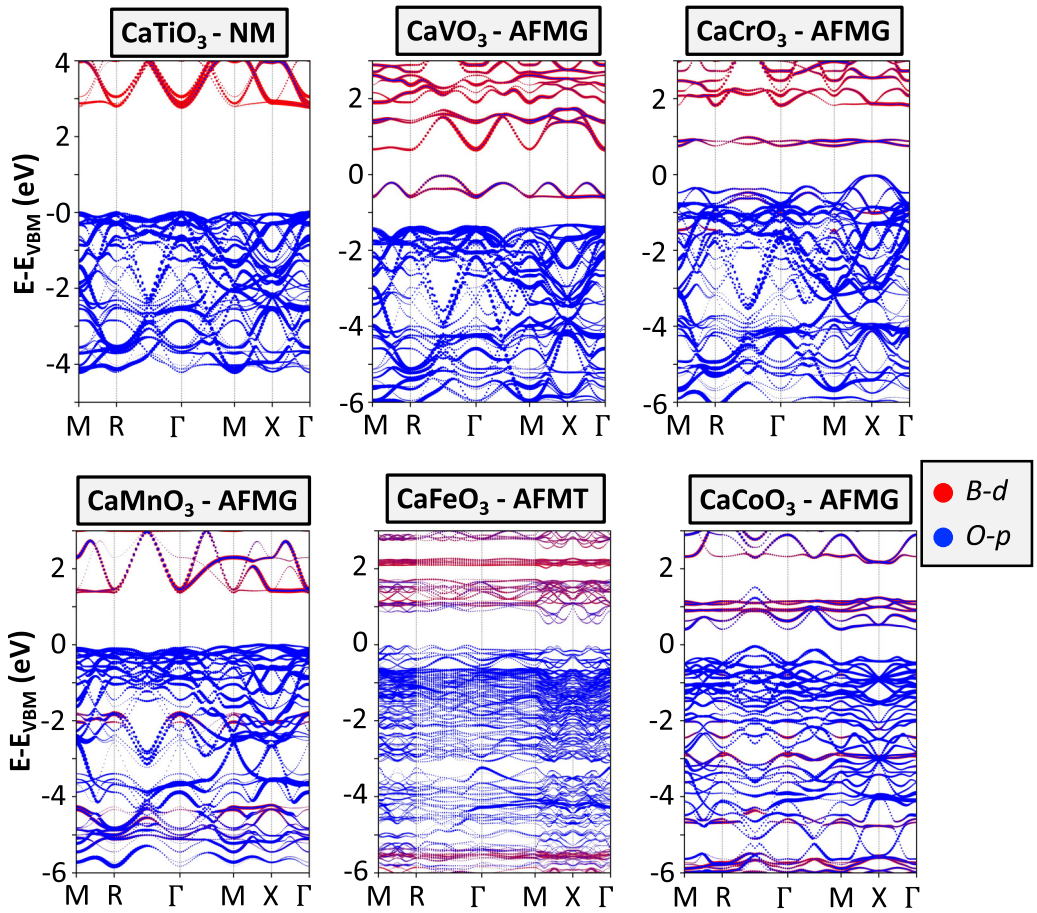

FIG. 10. Unfolded band structures of $CaBO_3$ compounds projected on the transition metal B *d* states (in red) and O *p* states (in blue). DFT+U results are used here. Only the majority spin channel is reported.

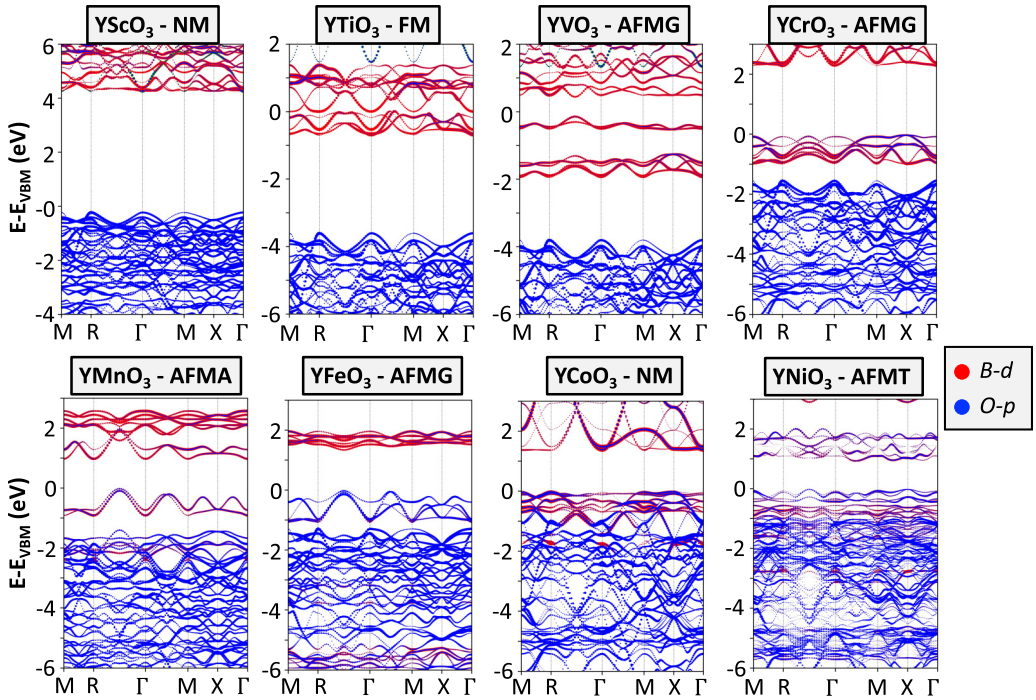

FIG. 11. Unfolded band structures of YBO_3 compounds projected on the transition metal B *d* states (in red) and O *p* states (in blue). SCAN results are used here. Only the majority spin channel is reported.

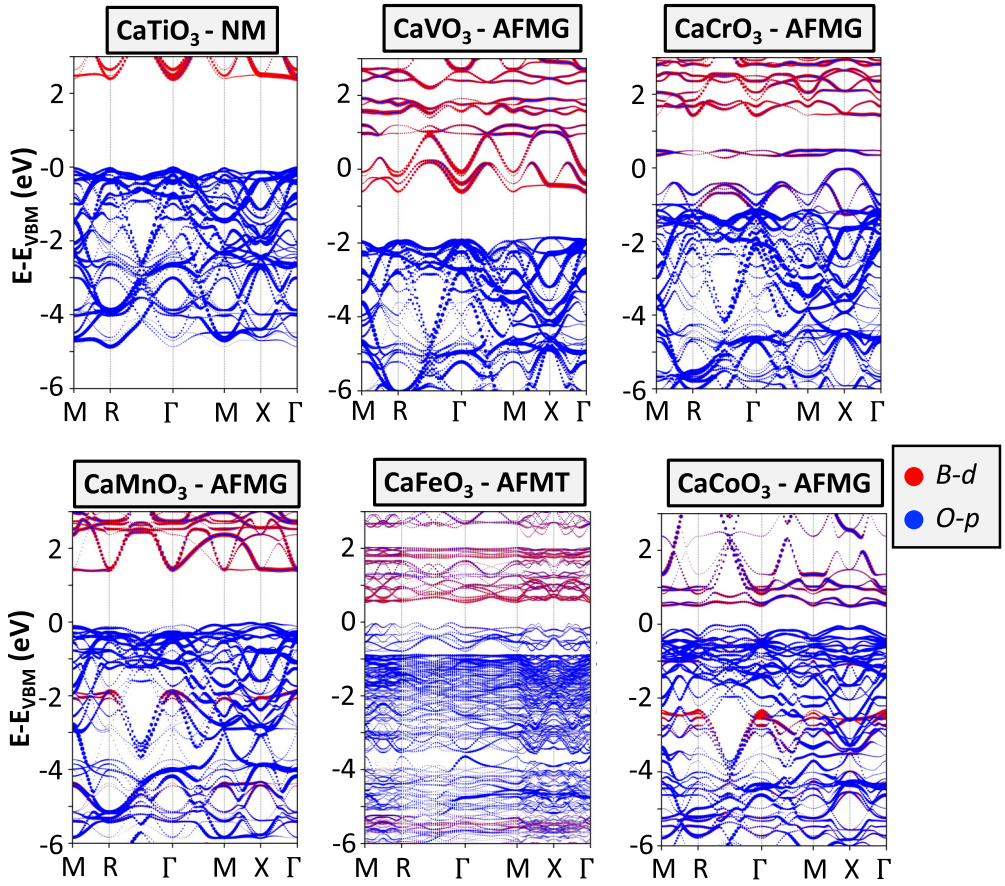

FIG. 12. Unfolded band structures of $CaBO_3$ compounds projected on the transition metal B *d* states (in red) and O *p* states (in blue). SCAN results are used here. Only the majority spin channel is reported.

All drawbacks related to gap properties might be circumvented by using an appropriate antiferromagnetic order in *first-principles* simulations, notably in charge-transfer insulators.

ACKNOWLEDGMENTS

J.V. acknowledges access granted to HPC resources of Criann through Projects No. 2020005 and No. 2007013 and of Cines through DARI Project No. A0080911453. Work at University of Colorado Boulder was supported under the NSF, Division of Materials Research, Condensed Matter and Materials Theory program, Grant No. DMR 2113922. A.Z. thankfully acknowledges discussions with G. Sawatzky on this subject.

APPENDIX: BAND EDGE ORBITAL CHARACTER FOR ABO_3 COMPOUNDS

We report in Figs. 9–12 the unfolded band structures of the different tested compounds in their experimentally reported magnetic states at low temperature using both the PBEsol+U and SCAN functionals. These band structures are projected on the transition metal *d* states and O *p* states allowing us to extract the band edge character. The points of the primitive Brillouin zone in the *Pm*-3*m* cell are Γ (0,0,0), X(1/2,0,0), M (1/2,1/2,0), and R(1/2,1/2,1/2).

[1] M. Coll, J. Fontcuberta, M. Althammer, M. Bibes, H. Boschker, A. Calleja, G. Cheng, M. Cuoco, R. Dittmann, B. Dkhil, I. El Baggari, M. Fanciulli, I. Fina, E. Fortunato, C. Frontera, S. Fujita, V. Garcia, S. T. B. Goennenwein, C. G. Granqvist, J. Grollier, R. Gross, A. Hagfeldt, G. Herranz, K. Hono, E. Houwman, M. Huijben, A. Kalaboukhov, D. J. Keeble, G. Koster, L. F. Kourkoutis, J. Levy, M. Lira-Cantu, J. L. MacManus-Driscoll, J. Mannhart, R. Martins, S. Menzel, T. Mikolajick, M. Napari, M. D. Nguyen, G. Niklasson, C. Paillard, S. Panigrahi, G. Rijnders, F. Sánchez, P. Sanchis, S. Sanna, D. G. Schlom, U. Schroeder, K. M. Shen, A. Siemon, M. Spreitzer, H. Sukegawa, R. Tamayo, J. van den Brink, N. Pryds, and F. M. Granozio, Appl. Surf. Sci. **482**, 1 (2019).

[2] M. Imada, A. Fujimori, and Y. Tokura, Rev. Mod. Phys. **70**, 1039 (1998).

[3] J. H. Ngai, F. J. Walker, and C. H. Ahn, Annu. Rev. Mater. Res. **44**, 1 (2014).

[4] N. F. Mott and Z. Zinamon, Rep. Prog. Phys. **33**, 881 (1970).
[5] N. Mott, *Metal-Insulator Transitions* (CRC, Boca Raton, FL, 1990).
[6] N. D. Ashcroft and N. W. Mermin, *Solid State Physics* (Saunders College, USA, 1976).
[7] J. Hubbard, Proc. R. Soc. A **276**, 238 (1963).
[8] J. Hubbard, Proc. R. Soc. A **281**, 401 (1964).
[9] J. C. Slater, Phys. Rev. **82**, 538 (1951).
[10] I. Lo Vecchio, A. Perucchi, P. Di Pietro, O. Limaj, U. Schade, Y. Sun, M. Arai, K. Yamaura, and S. Lupi, Sci. Rep. **3**, 2990 (2013).
[11] G. Trimarchi, Z. Wang, and A. Zunger, Phys. Rev. B **97**, 035107 (2018).
[12] G. M. Dalpian, Q. Liu, J. Varignon, M. Bibes, and A. Zunger, Phys. Rev. B **98**, 075135 (2018).
[13] T. Thonhauser and K. M. Rabe, Phys. Rev. B **73**, 212106 (2006).
[14] O. I. Malyi and A. Zunger, Appl. Phys. Rev. **7**, 041310 (2020).
[15] K. Foyevtsova, A. Khazraie, I. Elfimov, and G. A. Sawatzky, Phys. Rev. B **91**, 121114(R) (2015).
[16] A. Khazraie, K. Foyevtsova, I. Elfimov, and G. A. Sawatzky, Phys. Rev. B **97**, 075103 (2018).
[17] J. Varignon, M. Bibes, and A. Zunger, Nat. Commun. **10**, 1658 (2019).
[18] J. Varignon, M. Bibes, and A. Zunger, Phys. Rev. B **100**, 035119 (2019).
[19] Y. Zhang, J. Furness, R. Zhang, Z. Wang, A. Zunger, and J. Sun, Phys. Rev. B **102**, 045112 (2020).
[20] J. Zaanen, G. A. Sawatzky, and J. W. Allen, Phys. Rev. Lett. **55**, 418 (1985).
[21] D. I. Khomskii, *Transition Metal Compounds* (Cambridge University, New York, 2014).
[22] J. Varignon, M. Bibes, and A. Zunger, Phys. Rev. Res. **1**, 033131 (2019).
[23] A. Mercy, J. Bieder, J. Íñiguez, and P. Ghosez, Nat. Commun. **8**, 1677 (2017).
[24] H. Xiang, C. Lee, H. J. Koo, X. Gong, and M. H. Whangbo, Dalt. Trans. **42**, 823 (2013).
[25] J. He and C. Franchini, Phys. Rev. B **86**, 235117 (2012).
[26] G. Kresse and J. Haffner, Phys. Rev. B **47**, 558 (1993).
[27] G. Kresse and J. Furthmüller, J. Comput. Mater. Sci. **6**, 15 (1996).
[28] J. P. Perdew, A. Ruzsinszky, G. I. Csonka, O. A. Vydrov, G. E. Scuseria, L. A. Constantin, X. Zhou, and K. Burke, Phys. Rev. Lett. **100**, 136406 (2008).
[29] S. L. Dudarev, G. A. Botton, S. Y. Savrasov, C. J. Humphreys, and A. P. Sutton, Phys. Rev. B **57**, 1505 (1998).
[30] R. M. Martin, *Electronic Structure: Basic Theory and Practical Methods* (Cambridge University, New York, 2004).
[31] J. Sun, A. Ruzsinszky, and J. Perdew, Phys. Rev. Lett. **115**, 036402 (2015).
[32] B. L. Chamberland and P. S. Danielson, J. Solid State Chem. **3**, 243 (1971).
[33] J. S. Zhou, C. Q. Jin, Y. W. Long, L. X. Yang, and J. B. Goodenough, Phys. Rev. Lett. **96**, 046408 (2006).
[34] A. C. Komarek, S. V. Streltsov, M. Isobe, T. Möller, M. Hoelzel, A. Senyshyn, D. Trots, M. T. Fernández-Díaz, T. Hansen, H. Gotou, T. Yagi, Y. Ueda, V. I. Anisimov, M. Grüninger, D. I. Khomskii, and M. Braden, Phys. Rev. Lett. **101**, 167204 (2008).
[35] A. M. Glazer, Acta Crystallogr. Sect. B **28**, 3384 (1972).
[36] P. E. Blöchl, Phys. Rev. B **50**, 17953 (1994).
[37] D. Orobengoa, C. Capillas, I. Aroyo, and J. M. Perez, J. Appl. Crystallogr. **42**, 820 (2009).
[38] J. M. Perez-Mato, D. Orobengoa, and M. I. Aroyo, Acta Crystallogr. Sect. A **66**, 558 (2010).
[39] V. Popescu and A. Zunger, Phys. Rev. B **85**, 085201 (2012).
[40] A. A. Mostofi, J. R. Yates, Y.-S. Lee, I. Souza, D. Vanderbilt, and N. Marzari, Comput. Phys. Commun. **178**, 685 (2008).
[41] N. Marzari and D. Vanderbilt, Phys. Rev. B **56**, 12847 (1997).
[42] I. Souza, N. Marzari, and D. Vanderbilt, Phys. Rev. B **65**, 035109 (2001).
[43] J. Kanamori, J. Phys. Chem. Solids **10**, 87 (1959).
[44] M. Ekholm, D. Gambino, H. J. M. Jönsson, F. Tasnádi, B. Alling, and I. A. Abrikosov, Phys. Rev. B **98**, 094413 (2018).
[45] Y. Fu and D. J. Singh, Phys. Rev. Lett. **121**, 207201 (2018).
[46] Y. Zhang, M. M. Schmitt, A. Mercy, J. Wang, and P. Ghosez, Phys. Rev. B **98**, 081108(R) (2018).
[47] M. M. Schmitt, Y. Zhang, Y. Zhang, A. Mercy, and P. Ghosez, Phys. Rev. B **101**, 214304 (2020).
[48] J. Varignon, N. C. Bristowe, E. Bousquet, and P. Ghosez, Sci. Rep. **5**, 15364 (2015).
[49] J. Varignon, N. C. Bristowe, and P. Ghosez, Phys. Rev. Lett. **116**, 057602 (2016).
[50] J. B. Goodenough, J. Phys. Chem. Solids **6**, 287 (1958).
[51] M. H. Sage, G. R. Blake, C. Marquina, and T. T. M. Palstra, Phys. Rev. B **76**, 195102 (2007).
[52] S. Miyasaka, Y. Okimoto, M. Iwama, and Y. Tokura, Phys. Rev. B **68**, 100406 (2003).
[53] K. I. Kugel and D. I. Khomskii, Sov. Phys. JETP **64**, 1429 (1973).
[54] K. I. Kugel and D. I. Khomskii, Sov. Phys. Usp. **25**, 231 (1982).
[55] S. Catalano, M. Gibert, J. Fowlie, J. Iñiguez, J. M. Triscone, and J. Kreisel, Reports Prog. Phys. **81**, 046501 (2018).
[56] G. Catalan, Phase Transition **81**, 729 (2008).
[57] A. Subedi, O. E. Peil, and A. Georges, Phys. Rev. B **91**, 075128 (2015).
[58] A. Hampel, P. Liu, C. Franchini, and C. Ederer, npj Quantum Mater. **4**, 5 (2019) .
[59] A. Jain, S. P. Ong, G. Hautier, W. Chen, W. D. Richards, S. Dacek, S. Cholia, D. Gunter, D. Skinner, G. Ceder, and K. A. Persson, APL Mater. **1**, 011002 (2013).
[60] J. E. Saal, S. Kirklin, M. Aykol, B. Meredig, and C. Wolverton, JOM **65**, 1501 (2013).
[61] S. Kirklin, J. E. Saal, B. Meredig, A. Thompson, J. W. Doak, M. Aykol, S. Rühl, and C. Wolverton, npj Comput. Mater. **1**, (2015).
[62] S. Curtarolo, W. Setyawan, G. L. W. Hart, M. Jahnatek, R. V. Chepulskii, R. H. Taylor, S. Wang, J. Xue, K. Yang, O. Levy, M. J. Mehl, H. T. Stokes, D. O. Demchenko, and D. Morgan, Comput. Mater. Sci. **58**, 218 (2012).